

^{12}CO emission from EP Aquarii: Another example of an axi-symmetric AGB wind?★

P. T. Nhung^{1,2}, D. T. Hoai^{1,2}, J. M. Winters³, T. Le Bertre¹, P. N. Diep², N. T. Phuong², N. T. Thao²,
P. Tuan-Anh², and P. Darriulat²

¹ LERMA, UMR 8112, CNRS & Observatoire de Paris/PSL, 61 Av. de l'Observatoire, 75014 Paris, France
e-mail: nhung.pham@obspm.fr

² Department of Astrophysics, Vietnam National Satellite Center, VAST, 18 Hoang Quoc Viet, Ha Noi, Vietnam

³ IRAM, 300 rue de la Piscine, Domaine Universitaire, 38406 St.-Martin d'Hères, France

Received 18 May 2015 / Accepted 6 August 2015

ABSTRACT

The CO(1–0) and (2–1) emission of the circumstellar envelope of the asymptotic giant branch (AGB) star EP Aqr has been observed in 2003 using the IRAM Plateau-de-Bure Interferometer and in 2004 with the IRAM 30-m telescope at Pico Veleta. The line profiles reveal the presence of two distinct components centred on the star velocity, a broad component extending up to $\sim 10 \text{ km s}^{-1}$ and a narrow component indicating an expansion velocity of only $\sim 2 \text{ km s}^{-1}$. An early analysis of these data was performed under the assumption of isotropic winds. The present study revisits this interpretation, instead assuming a bipolar outflow nearly aligned with the line of sight. A satisfactory description of the observed flux densities is obtained with a radial expansion velocity increasing from $\sim 2 \text{ km s}^{-1}$ at the equator to $\sim 10 \text{ km s}^{-1}$ near the poles. The mass-loss rate is $\sim 1.2 \times 10^{-7} M_{\odot} \text{ yr}^{-1}$. The angular aperture of the bipolar outflow is $\sim 45^{\circ}$ with respect to the star axis, which makes an angle of $\sim 13^{\circ}$ with the line of sight. A detailed study of the CO(1–0) to CO(2–1) flux ratio reveals a significant dependence of the temperature on the stellar latitude, smaller and steeper at the poles than at the equator at large distances from the star ($>2'' \equiv 1.0 \times 10^{-3} \text{ pc}$). Under the hypothesis of radial expansion of the gas and of rotation invariance about the star axis, the effective density was evaluated in space as a function of star coordinates (longitude, latitude, and distance from the star). Evidence is found for an enhancement of the effective density in the northern hemisphere of the star at angular distances in excess of $\sim 3''$ and covering the whole longitudinal range. The peak velocity of the narrow component is observed to vary slightly with position on the sky, a variation consistent with the model and understood as the effect of the inclination of the star axis with respect to the line of sight. This variation is inconsistent with the assumption of a spherical wind and strengthens our interpretation in terms of an axisymmetric outflow. While the phenomenological model presented here reproduces well the general features of the observations, not only qualitatively but also quantitatively, significant differences are also revealed, which would require a better spatial resolution to be properly described and understood.

Key words. stars: AGB and post-AGB – circumstellar matter – stars: individual: EP Aquarii – stars: mass-loss – radio lines: stars

1. Introduction

EP Aqr is one of the nearest mass losing asymptotic giant branch (AGB) stars ($d = 114 \text{ pc}$, van Leeuwen 2007), and as such one of the best characterized objects of its class. The absence of technetium in the spectrum (Lebzelter & Hron 1999), and the low value of the $^{12}\text{C}/^{13}\text{C}$ abundance ratio (~ 10 , Cami et al. 2000) indicate that it is still at the beginning of its evolution on the AGB. Yet *Herschel* has imaged a large scale ($2' \times 4'$) circumstellar shell at $70 \mu\text{m}$ (Cox et al. 2012) testifying to a relatively long duration of the mass loss ($>10^4 \text{ yr}$) and to interaction with the surrounding interstellar medium. The elongation of the far-infrared image is in a direction opposite to the EP Aqr space motion. From HI observations at 21 cm, Le Bertre & Gérard (2004) estimate a duration of $\sim 1.6 \times 10^5 \text{ yr}$ for the present episode of mass loss.

Combined observations have been obtained with the IRAM 30-m telescope and the Plateau-de-Bure Interferometer in $^{12}\text{CO}(1-0)$ and $^{12}\text{CO}(2-1)$ in 2003 and 2004, improving over

earlier observations (Knapp et al. 1998; Nakashima 2006). The spectra, which reveal a wind composed of two main components with expansion velocities ~ 2 and $\sim 10 \text{ km s}^{-1}$, were analyzed in terms of multiple isotropic winds (Winters et al. 2003, 2007). The interferometer data show an extended source of about $15''$ (FWHM), and evidence for a ring structure in CO(2–1). However, when assuming multiple isotropic winds, Winters et al. (2007) did not manage to fully explain the line profiles obtained at different positions of the spectral maps.

Composite CO line profiles have been observed for several AGB sources, including RS Cnc and X Her (e.g. Knapp et al. 1998). Kahane & Jura (1996) interpreted the narrow line component of X Her in terms of a spherically expanding wind and the broad line component in terms of a bipolar flow, probably observed at a viewing angle of about 15° . For RS Cnc, high spatial resolution observations can be interpreted assuming the same geometry but with a different inclination of about 40° with respect to the line of sight (Hoai et al. 2014). These results raise the question whether the bipolar outflow hypothesis might also apply to EP Aqr.

The present study is therefore revisiting the analysis of Winters et al. (2007), instead assuming a bipolar outflow

★ Based on observations carried out with the IRAM Plateau-de-Bure Interferometer and the IRAM 30-m telescope. IRAM is supported by INSU/CNRS (France), MPG (Germany), and IGN (Spain).

approximately directed along the line of sight. We exploit the experience gained in similar studies of other stars, RS Cnc (Hoi et al. 2014; Nhung et al. 2015) and the Red Rectangle, a post-AGB source, which could be interpreted by applying a similar model (Tuan Anh et al. 2015).

The paper is organized as follows: in Sect. 2 we present reprocessed data on EP Aqr, which is used in this work. Section 3 describes, in an elementary way, the main features implied by the assumed orientation of EP Aqr, with the star axis nearly parallel to the line of sight, mimicking spherical symmetry. Section 4 presents an analysis of the data using a simple bipolar outflow model that had been developed earlier for RS Cnc (Hoi et al. 2014; Nhung et al. 2015); the results of the best fit to the observations is used as a reference in the following sections. Section 5 presents a study of the CO(1–0) to CO(2–1) emission ratio, allowing for an evaluation of the temperature distribution nearly independent of the model adopted for the description of the gas density and velocity. Section 6 uses the distribution of the gas velocity obtained in Sect. 4 to reconstruct directly in space the effective gas density, without making direct use of the parametrization of the flux of matter obtained in Sect. 4, and, therefore, providing a consistency check of the results of the model. Finally, Sect. 7 presents a detailed study of the spatial variation of the radial velocity of the narrow line component. This last section, before the discussion and conclusion, provides a sensitive check of the bipolar outflow hypothesis and of its small inclination angle with respect to the line of sight.

2. Observations

The observations analysed here combine interferometer data obtained using the Plateau-de-Bure Interferometer with short-spacing data obtained using the Pico Veleta 30-m telescope. A detailed description of the original observations is given in Winters et al. (2007). $^{12}\text{CO}(2-1)$ and $^{12}\text{CO}(1-0)$ spectral data have been obtained with a spatial resolution of $\sim 1''$ and $\sim 2''$, respectively, and a spectral resolution of 0.1 km s^{-1} . At this spatial resolution, the two spectral components present in the single-dish line spectra are seen as originating from the same region. The images are virtually circularly symmetric and display smooth variations with velocity and projected distance from the star. In Winters et al. (2007), the observed spectra were interpreted by a succession of spherically symmetric and short-spaced mass-loss events. These authors noted the presence of inhomogeneities in the spectral maps indicating a possible clumpiness of the circumstellar envelope.

We reprocessed the original data, correcting for an artifact introduced by a velocity shift of 0.52 km s^{-1} in the CO(1–0) data and recentering the maps on the position of the star at epoch 2004.0, correcting for its proper motion as determined by van Leeuwen (2007). The reprocessed channel maps are shown in Figs. 1 and 2.

3. Observing a star along its symmetry axis

The high degree of azimuthal symmetry observed in the channel maps of both CO(1–0) and CO(2–1) emission (see Figs. 1 and 2, Winters et al. 2007) implies that a bipolar outflow, if present, should have its axis nearly parallel to the line of sight. In this kind of configuration, some simple relations apply between the space coordinates and their projection on the sky plane. We review them briefly to clarify further discussion. We use coordinates (Fig. 3) centred on the star with x along the star axis, parallel to the line of sight, y pointing east and z pointing north. We

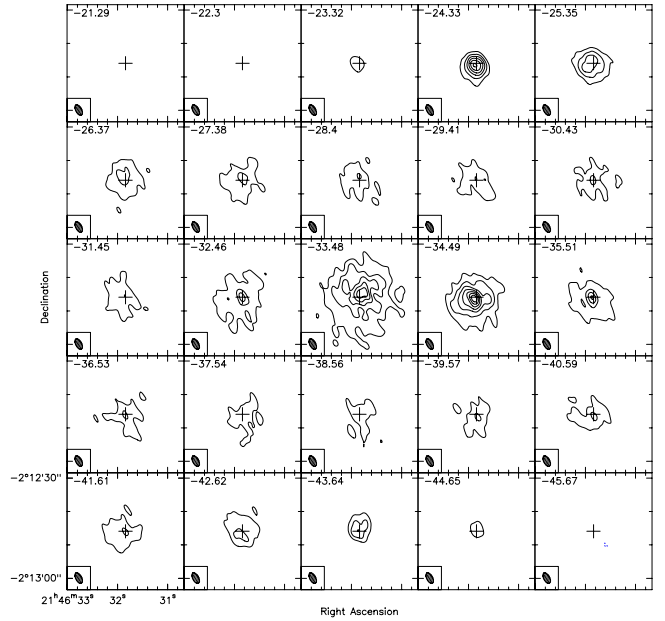


Fig. 1. Channel maps in the $^{12}\text{CO}(J = 1-0)$ line (smoothed to a width of 1 km s^{-1}). Contours are plotted at 5, 10, 20, 30, 40σ ($1\sigma = 14 \text{ mJy/beam}$). The synthesized beam is indicated at the lower left corner of each panel.

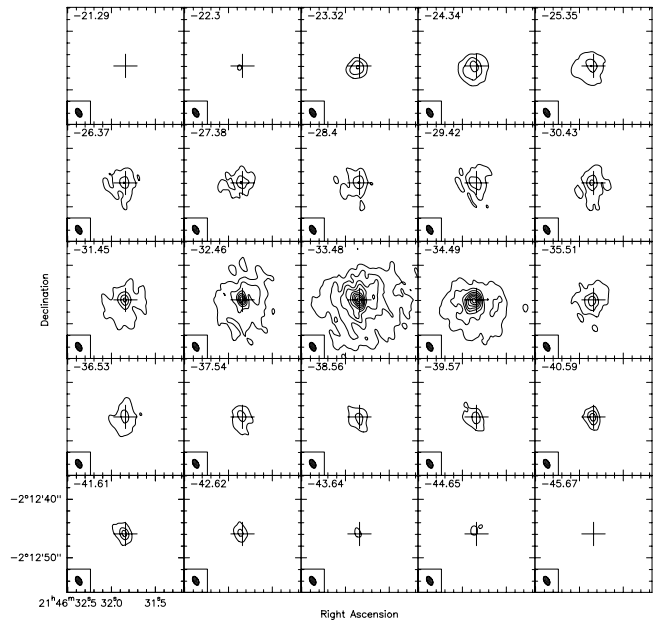


Fig. 2. Channel maps in the $^{12}\text{CO}(J = 2-1)$ line (smoothed to a width of 1 km s^{-1}). First contour is plotted at 10σ , the following contours start at 20σ and are plotted in 20σ steps ($1\sigma = 16 \text{ mJy/beam}$). The synthesized beam is indicated at the lower left corner of each panel.

assume rotation symmetry about the x axis and symmetry about the equatorial (y, z) plane of the star. Defining ρ as the gas density, T the gas temperature, and \mathbf{V} the gas velocity in the star rest frame, having components V_x, V_y, V_z , the following relations apply at point (x, y, z) : ρ and T are functions of $r = (x^2 + y^2 + z^2)^{1/2}$ and of $|\alpha|$, where $\alpha = \arctan(x/R)$ is the latitude in the star reference system, and $R = (y^2 + z^2)^{1/2}$ is the projection of r on the sky plane.

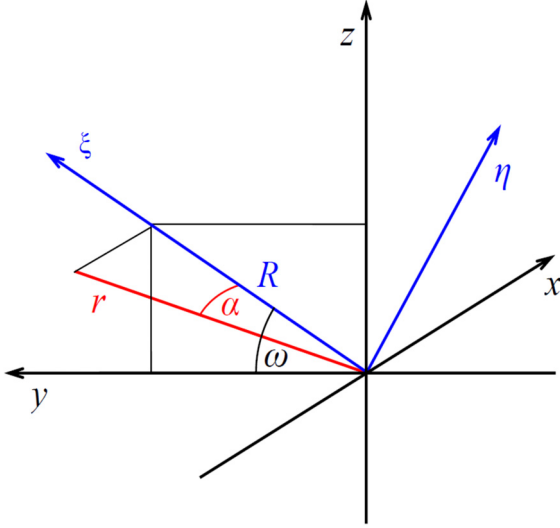


Fig. 3. Definition of coordinates. The (ξ, η) coordinates are obtained from (y, z) coordinates by rotation of angle ω in the sky plane about the x axis (line of sight and star axis, cf. Sect. 3). In the sky plane, y is towards east, and z towards north.

The velocity V takes a simple form when expressed in terms of meridian coordinates, $R = y \cos \omega + z \sin \omega$, x and $\eta = -y \sin \omega + z \cos \omega$, ω is the stellar longitude; its components are then functions of r and $|\alpha|$. In case of pure radial expansion, $V_\eta = 0$, $V_x = xV/r$, and $V_R = RV/r$, while in case of pure rotation $V_R = V_x = 0$.

In the case of pure radial expansion with a known radial dependence of the velocity, the flux density f measured in a pixel (y, z) at velocity V_x is associated with a well-defined position in space, obtained from

$$x = rV_x/V = (x^2 + R^2)^{\frac{1}{2}} V_x/V = RV_x (V^2 - V_x^2)^{-\frac{1}{2}}. \quad (1)$$

Then, if one knows V , one can calculate V_x and, therefore, its derivative dV_x/dx at any point in space. Defining an effective density ρ_{eff} as $\rho_{\text{eff}} = f dV_x/dx$, such that the observed flux in a given pixel be $\int f dV_x = \int \rho_{\text{eff}} dx$, one is then able to calculate it at any point in space. The effective density, defined by this relation, is the product of the actual gas density and a factor accounting for the population of the emitting state, the emission probability, and correcting for the effect of absorption.

We illustrate the above properties with a simple example, close to the reality of EP Aqr. We assume exact rotation invariance about the star axis (parallel to the line of sight), a purely radial wind with a velocity that only depends on α , i.e.

$$V = V_0 + V_1 \sin^2 \alpha \quad (2)$$

(V_0 at the equator and $V_0 + V_1$ at the poles) and an effective density (defined such that its integral over the line of sight measures the observed flux density) inversely proportional to r^2 . From $V_x = V \sin \alpha$ and Eq. (2), we obtain $\sin^3 \alpha + (V_0/V_1) \sin \alpha - (V_x/V_1) = 0$. This reduced cubic equation is explicitly solvable with $\sin \alpha = -(q-s)^{\frac{1}{3}} - (q+s)^{\frac{1}{3}}$, $s = (q^2 + p^3)^{\frac{1}{2}}$, $p = \frac{1}{3} V_0/V_1$, and $q = -\frac{1}{2} V_x/V_1$. For a given value of the Doppler velocity V_x , one can therefore calculate α independent of R : in any pixel, V_x and α are therefore related in a unique way, which is illustrated in Fig. 4 (upper panel). Similarly, V_x and $r/R = 1/\cos \alpha$ are also related in a universal way, independent of R (Fig. 4, middle panel). The resulting velocity spectra are indicated in Fig. 4

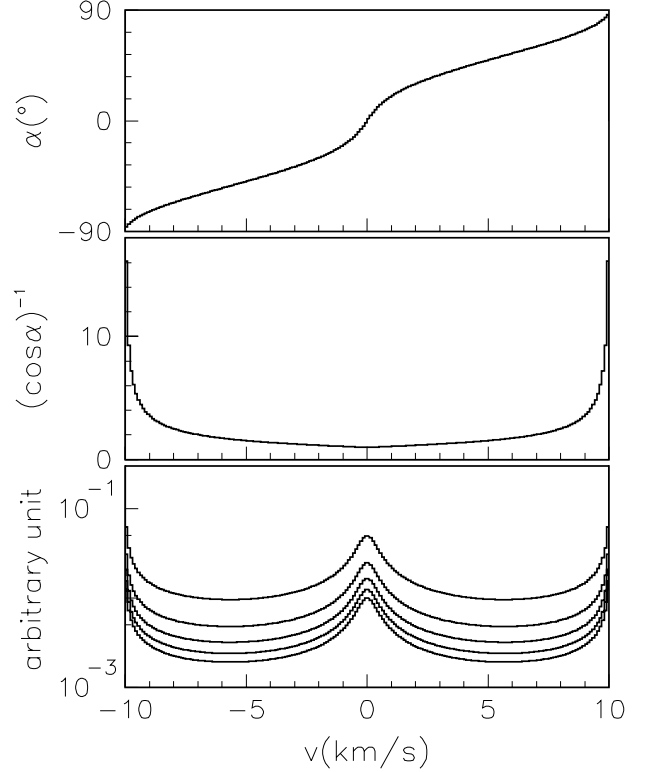


Fig. 4. Relation between the Doppler velocity V_x and the stellar latitude α (cf. Eq. (2), upper panel), the ratio $r/R = 1/\cos \alpha$ (middle panel) for the simple star model described in the text. Lower panel: velocity spectra obtained for the same model at $R = 1-5$ (running downwards).

(lower panel) for $R = 1, 2, 3, 4$, and 5 (all quantities are in arbitrary units except for the velocities, which are in km s^{-1} with $V_0 = 2 \text{ km s}^{-1}$ and $V_1 = 8 \text{ km s}^{-1}$). They simply scale as $1/R$, reflecting the $1/r^2$ dependence of the effective density. In a simple model like this, the flux ratio between the CO(1–0) and CO(2–1) is a constant, independent of R and V_x .

4. Comparison of the observations with a bipolar outflow model

The spectral maps extracted from the reprocessed data (see Sect. 2) are shown in Fig. 5. The spectra are shown in steps of $1''$ in right ascension and declination. The synthesized beam is $3.53'' \times 1.84''$ (PA = 28°) for CO(1–0), and $1.67'' \times 0.94''$ (PA = 29°) for CO(2–1), respectively.

To describe EP Aqr, we use the model of Hoai et al. (2014), which assumes that the wind is purely radial, free of turbulence, and in local thermal equilibrium. For solving the radiative transfer, a ray-tracing method that takes absorption into account is used (Hoai, in prep.). Moreover, the wind is assumed to be stationary and is supposed to have been in this kind of regime for long enough so that the radial extension of the gas volume is governed exclusively by the UV dissociation of the CO molecules by interstellar radiation (Mamon et al. 1988) and does not keep any trace of the star history. For EP Aqr, the CO/H abundance ratio is taken as 2.5×10^{-4} (Knapp et al. 1998), a value representative for an M-type star. The temperature is parametrized by a power law of r , $T = T_0 r^{-n}$ but is independent of the stellar latitude α . The spectrum of flux densities in each pixel is calculated via integration along the line of sight, the temperature dependent contributions of emission and absorption being

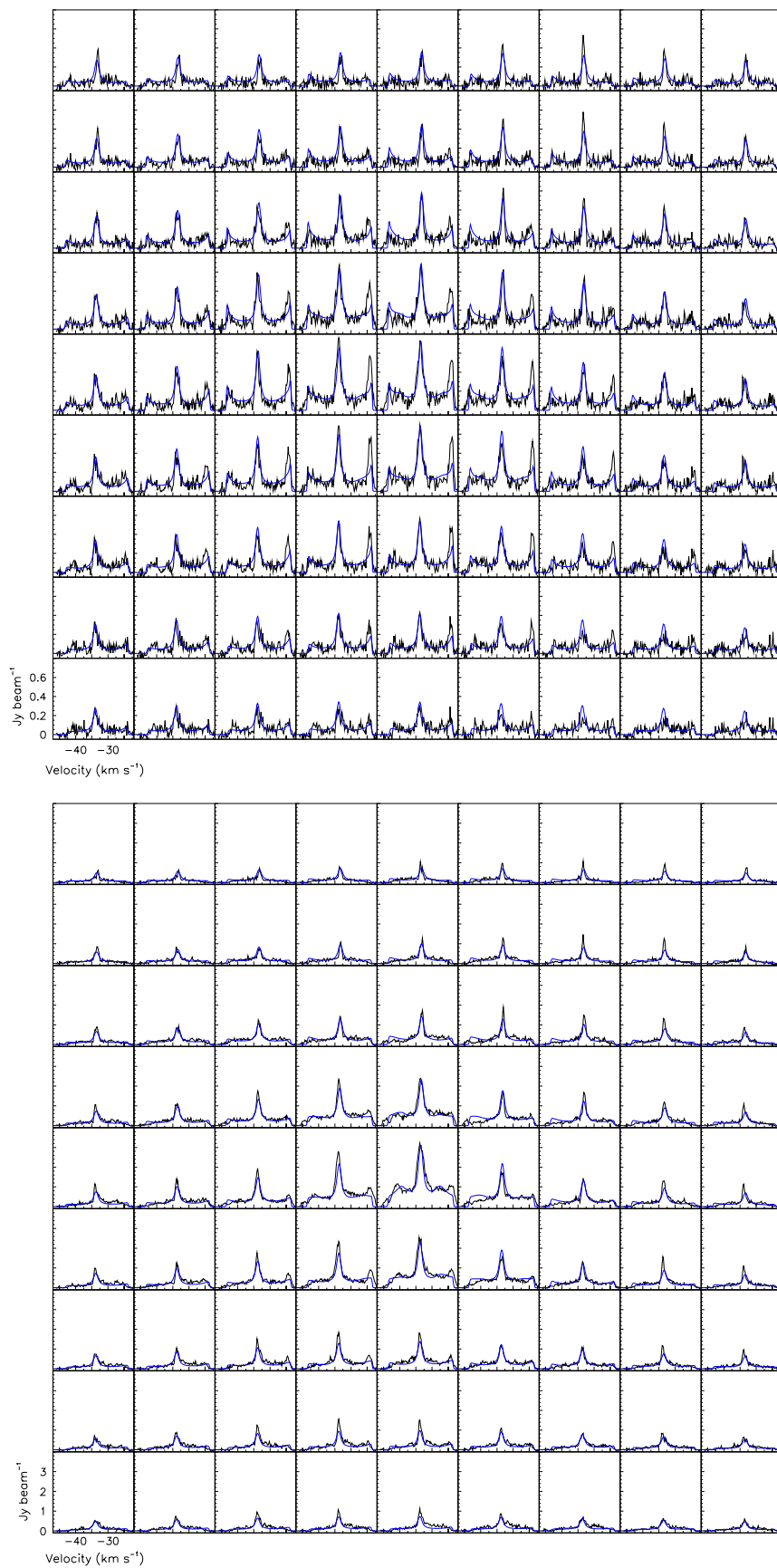


Fig. 5. Spectral maps centred on the star of the CO observations (black) and the best-fit model (blue). The CO(1–0) map is shown in the *upper panel*, CO(2–1) in the *lower panel*. Steps in right ascension and declination are 1″.

Table 1. Best-fit parameters obtained for the CO(1–0) and CO(2–1) data. A distance of 114 pc is adopted.

Parameter	Best-fit value
θ	13°
ψ	144°
σ	0.3
V_1	8.0 km s^{-1}
V_2	2.0 km s^{-1}
f_{M_1}	$1.26 \times 10^{-8} M_\odot \text{ yr}^{-1} \text{ sr}^{-1}$
f_{M_2}	$0.49 \times 10^{-8} M_\odot \text{ yr}^{-1} \text{ sr}^{-1}$
λ_1	0.52
λ_2	0.38
$T_0 (r = 1'')$	116 K
n	0.77

respectively added and subtracted at each step. The wind velocity V and the flux of matter f_M are smooth functions of $|\sin \alpha|$ and an allowance is made for a radial velocity gradient described by parameters λ_1 at the poles and λ_2 at the equator. Assuming the wind is stationary, the density ρ is then defined at any point by the relation $f_M(\alpha) = r^2 \rho(\alpha, r) V(\alpha, r)$.

The bipolarity of the flow is parametrized as a function of $\sin \alpha$ using Gaussian forms centred at the poles,

$$G = \exp\left[-\frac{1}{2}(\sin \alpha - 1)^2/\sigma^2\right] + \exp\left[-\frac{1}{2}(\sin \alpha + 1)^2/\sigma^2\right], \quad (3)$$

where σ is a parameter to be adjusted. This function is used to define the $\sin \alpha$ dependence of both the wind velocity and the flux of matter, i.e.

$$V = V_1 G(1 - \lambda_1 e^{-r/2.5''}) + V_2 (1 - \lambda_2 e^{-r/2.5''}) \quad (4)$$

and

$$f_M = f_{M_1} G + f_{M_2}. \quad (5)$$

The density then results from mass conservation, i.e.

$$\rho = r^{-2}(f_{M_1} G + f_{M_2}) / [V_1 G(1 - \lambda_1 e^{-r/2.5''}) + V_2 (1 - \lambda_2 e^{-r/2.5''})]. \quad (6)$$

For r -independent wind velocities, $\lambda_1 = \lambda_2 = 0$, the velocity and flux of matter are nearly $V_1 + V_2$ and $f_{M_1} + f_{M_2}$ at the poles and $\varepsilon V_1 + V_2$ and $\varepsilon f_{M_1} + f_{M_2}$ at the equator, where ε is the small positive value taken by G at the equator.

We make allowance for a small inclination θ of the star axis with respect to the line of sight, with position angle ψ with respect to the north. The relations quoted in Sect. 3 for $\theta = 0$ are modified accordingly. More precisely, the position of the star frame with respect to the sky plane and line of sight is now defined by angles θ and ψ and the polar coordinates in the star frame are the latitude α and longitude ω defined to conform with the definition given in Sect. 3 for $\theta = 0$. The star radial velocity as determined from the CO line profiles is -33.5 km s^{-1} , which is in good agreement with the value of -34 km s^{-1} derived in Winters et al. (2003). The values taken by the parameters are obtained by a standard χ^2 minimization method. The best-fit values of the parameters of the model to the joint CO(1–0) and CO(2–1) observations are listed in Table 1 and the quality of the fit is illustrated in Fig. 5, where the modelled velocity spectra are superimposed over those observed.

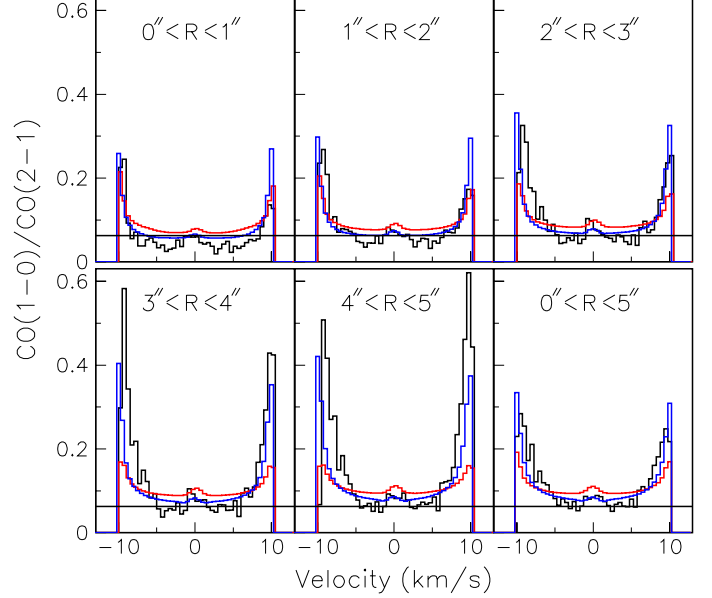


Fig. 6. CO(1–0) to CO(2–1) flux ratio (black) where each of the CO(1–0) and CO(2–1) fluxes has been averaged over five successive velocity bins and over the concentric rings defined in the text. The lower right panel indicates all pixels with $R < 5''$. The result of the best fit of the model described in Sect. 4 is shown in red and that of its modification described in Sect. 5 is shown in blue. The horizontal lines indicate the level (0.063) above which the data must lie, under the hypothesis of local thermal equilibrium.

This result shows that it is possible to describe the morphology and kinematics of the gas envelope of EP Aqr as the combination of a slow isotropic wind and a bipolar outflow, since the wind velocities at the equator and at the poles are $\sim 2 \text{ km s}^{-1}$ and $\sim 10 \text{ km s}^{-1}$, respectively, and the inclination of the star axis with respect to the line of sight, θ , is $\sim 13^\circ$. The flux of matter varies from $0.49 \times 10^{-8} M_\odot \text{ yr}^{-1} \text{ sr}^{-1}$ in the equatorial plane to $1.75 \times 10^{-8} M_\odot \text{ yr}^{-1} \text{ sr}^{-1}$ in the polar directions. The total mass-loss rate is $1.2 \times 10^{-7} M_\odot \text{ yr}^{-1}$. The angular aperture of the bipolar outflow, measured by the parameter $\sigma = 0.3$ in Eq. (3), corresponds to $\alpha = \arcsin(0.7) \sim 45^\circ$.

We leave a more detailed discussion of this result for Sect. 7. In the next section, we study the CO(1–0) to CO(2–1) flux ratio, which gives important information about the temperature distribution with only minimal dependence on the details of the model.

5. The CO(1–0) to CO(2–1) flux ratio

Comparing the fluxes associated with CO(1–0) and CO(2–1) emission provides information about the gas temperature nearly independently from the gas density and velocity, which are common to the two lines. In the optically thin limit and assuming local thermal equilibrium, the temperature T (K) is obtained from the ratio Q of the CO(1–0) to CO(2–1) fluxes as $T = 11.1/\ln(Q/0.063)$. However, the model presented in the preceding section does not reproduce the observed flux ratio well. In particular, we observe that Q is sometimes below the minimal value 0.063 allowed by the local thermal equilibrium hypothesis (when $T = \infty$). This is illustrated in Fig. 6, where the data have been averaged over concentric rings limited by circles with $R = 1''$ – $5''$, respectively.

Accordingly, we allow for a small difference of normalization between the CO(1–0) and CO(2–1) fluxes by multiplying

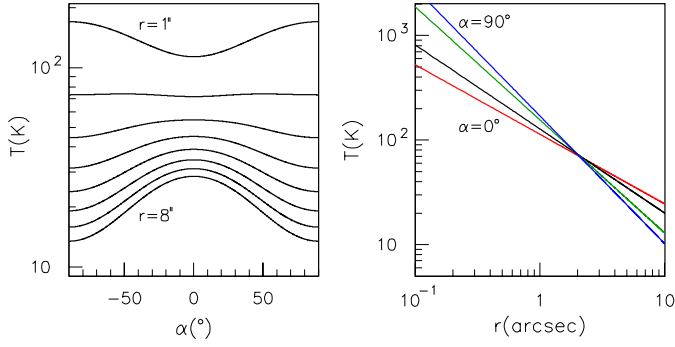


Fig. 7. Distribution of the gas temperature. *Left:* as a function of α at distances from the star $r = 1''$ to $8''$ (from top to bottom) in steps of $1''$; *right:* as a function of r at latitudes $\alpha = 0^\circ$ (red), 30° (black), 60° (green), and 90° (blue).

Table 2. Best-fit parameters of the CO(2–1) to CO(1–0) ratio.

Parameter	T_0 (K)	a	n_1	n_2	μ (%)	$\chi^2/\text{d.o.f.}$
Best-fit values	170	0.67	1.22	-0.55	9.0	1.14
Uncertainties	20	0.12	0.06	0.10	3.0	

the former by a factor $1 + \mu$ and the latter by a factor $1 - \mu$. This factor may account for a real difference in calibration as well as, in an ad hoc way, for any inadequacy of the model (assumption of local thermal equilibrium, absence of turbulence). Moreover, we see from Fig. 6 that one needs to increase the ratio Q near the extremities of the velocity spectrum more than in the middle, meaning near the poles at large values of r more than near the equator at small values of r . Accordingly, we parametrize the temperature in the form

$$T = T_0 (\sin^2 \alpha + a \cos^2 \alpha) (r/1'')^{-n} \quad (7)$$

with

$$n = n_1 + n_2 \cos^2 \alpha. \quad (8)$$

At $r = 1''$, the temperature is T_0 at the poles and aT_0 at the equator. The power index describing the radial dependence of the temperature is n_1 at the poles and $n_1 + n_2$ at the equator.

The result is summarized in Table 2 and illustrated in Fig. 7. The ratio between the values taken by the temperature at the equator and at the poles, ar^{-n_2} , varies from 0.70 at $r = 1''$ to 1.64 at $r = 5''$, crossing unity at $r \approx 2''$. As r/R is much larger near the poles than at the equator (it is equal to $1/\cos \alpha$ in the simple configuration studied in Sect. 3), the extremities of the velocity spectrum probe large r values, meaning low temperatures, as required by the measured Q values: both the values taken by n_2 and by a are determinant in increasing Q at the extremities of the velocity spectrum. For the same reason, the temperature increase obtained from the parametrization at small values of r and large values of α is not probed by any of the data, which makes its reliability uncertain.

The values of the temperature that we find close to the central star (~ 1000 K at $0.1''$) are consistent with those obtained by Cami et al. (2000) using infrared CO₂ lines.

The uncertainties listed in Table 2 are evaluated from the dependence of χ^2 over the values of the parameters, taking proper account of the correlations between them. However, they have been scaled up by a common factor such that the uncertainty in T_0 is 20 K. This somewhat arbitrary scaling is meant to cope

with our lack of detailed control over systematic errors and the value of 20 K is evaluated from the robustness of the results against changes of different nature that have been made to the model finally adopted in the course of the study. While the quoted uncertainties give a good idea of the reliability of the result and of its sensitivity to the values taken by the parameters, both the quality of the data (in particular the need for a μ -correction) and the crudeness of the model do not allow for a more serious quantitative evaluation.

We noted that the quality of the fits can be slightly improved by allowing for a temperature enhancement at mid-latitudes and small distances to the star; however, we were unable to establish the significance of this result with sufficient confidence.

The following two conclusions can then be retained:

- at large distances to the star, the temperature is significantly higher at the equator than at the poles, by typically 1 K at $r = 5''$;
- the temperature decreases with distance as $\sim r^{-1.2}$ at the poles and significantly less steeply at the equator, typically as $r^{-0.7}$.

6. Evaluation of the effective density in the star meridian plane

Under the hypotheses used to evaluate the model described in Sect. 4, one can associate to each data-triple (y, z, V_x) a point (r, α) in the meridian plane of the star. Indeed, x is a known function of r, α and the stellar longitude ω , as is $V_x = V_x/r$. The former uses the values of θ and ψ and the latter the parametrization of V as a function of r and α , which we obtained from the best fit. As one has three equations and three unknowns, one obtains r, α , and ω given V_x, y , and z . The flux density f corresponding to a given data-triple can therefore be mapped as an effective density $\rho_{\text{eff}} = f dV_x/dx$ in the meridian plane of the star, (i.e. each plane that contains the star's polar axis) with coordinates $r \cos \alpha$ and $r \sin \alpha$ (see Fig. 3). The evaluation of the flux density uses the best-fit parametrization of the wind velocity but not that of the flux of matter: therefore, it provides a consistency check.

We checked the validity of the procedure by replacing the data with the results of the model and verifying that the reconstructed effective density is identical to that used as input. The region of large $|\alpha|$ values is probed exclusively with the central pixels near the extremity of the spectrum and is therefore subject to large systematic uncertainties. Indeed, large $|\alpha|$ values mean large $|V_x|$ values, which in turn mean large r/R values, namely R is much smaller than r . For this reason, on the basis of the result of the validity check, we restrict the space reconstruction to pixels having $R > 1''$. In addition, to avoid dealing with fluxes that are too low, we require R not to exceed $10''$. The resulting maps of $r^2 \rho_{\text{eff}}$ are indicated in Fig. 8 for CO(1–0) and CO(2–1) separately and their averaged distributions as functions of r, α , and ω in Fig. 9.

All distributions display significant deviations with respect to the distributions generated by the model, which reproduces well the general trends, however. In principle, one should be able to include in the model the result of the space reconstruction of ρ_{eff} and iterate the fitting procedure with a more realistic parametrization of the flux of matter and possibly a more sophisticated velocity model. However, the quality of the present data is insufficient to undertake such an ambitious programme. We shall be satisfied with simply taking note of the differences between the model of Sect. 4 and the image revealed by the space reconstruction, as long as they can be considered both reliable and significant.

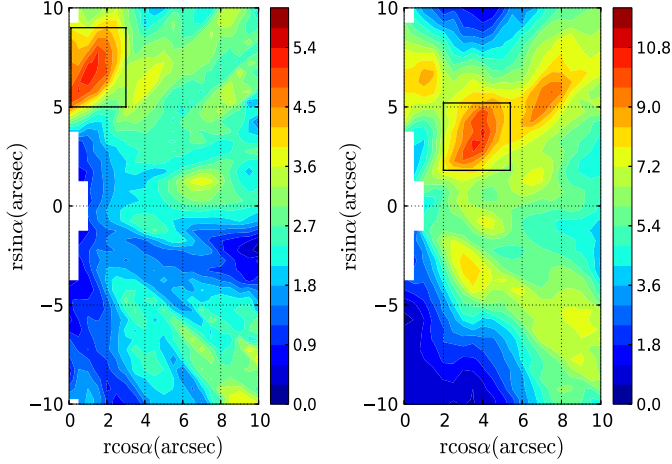


Fig. 8. Reconstructed maps of the effective density, multiplied by r^2 , in the star meridian plane under the assumption of a wind velocity having the form obtained from the best fit of the model described in Sect. 4. The colour codes are such that the ratio between maximum and minimum values of ρr^2 are the same for CO(1–0) (left) and CO(2–1) (right). Units are $\text{Jy beam}^{-1} \text{ km s}^{-1} \text{ arcsec}$. The rectangles show the regions selected for displaying the ω distributions shown in Fig. 10 (for CO(1–0), abscissa between $0''$ and $3''$, ordinate between $5''$ and $9''$; for CO(2–1), abscissa between $2.0''$ and $5.4''$, ordinate between $1.8''$ and $5.2''$).

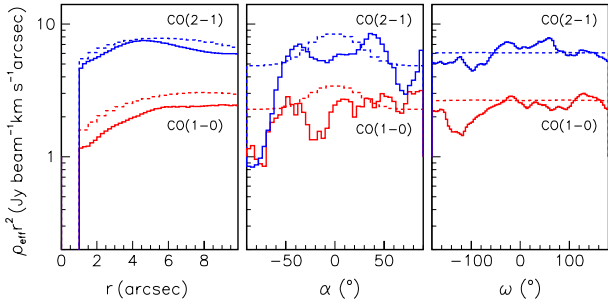


Fig. 9. Distributions of the average effective density, multiplied by r^2 , reconstructed in the meridian plane of the star for a wind velocity with the form obtained from the best fit of the model described in Sect. 4. The μ -correction has not been applied. *Left*: radial dependence of $r^2 \rho_{\text{eff}}$, averaged over α and ω ; *middle*: latitude dependence of $r^2 \rho_{\text{eff}}$, averaged over r and ω ; *right*: longitude dependence of $r^2 \rho_{\text{eff}}$, averaged over r and α . In each panel, CO(1–0) results are shown in red and CO(2–1) results in blue. The dashed curves show the results of the model, ignoring absorption.

The maps of Fig. 8 and the α distributions of Fig. 9 give evidence for a significant asymmetry between the northern and southern hemispheres of the star (defining north and south in the star coordinate system, north corresponding to $\alpha = \pi/2$, away from Earth). Indeed, a modification of the model allowing for an asymmetry of the same form as used in Nhung et al. (2015) for RS Cnc, namely multiplying the flux of matter by a common factor $1 + \gamma \sin \alpha$, gives a 20% excess in the northern hemisphere of the star. Differentiating between the asymmetries of the two mass-loss terms, $f_{M_1} G$ and f_{M_2} , reveals a strong correlation between them and the asymmetry of the first term is more efficient at improving the quality of the fit. Restricting the asymmetry to the first term results in a 37% excess in the northern hemisphere. The effect of absorption does not exceed $\sim 5\%$ on average and cannot be invoked to explain such asymmetry. The fluctuations observed in the distributions of the effective density, as well as the differences observed between the CO(1–0) and CO(2–1) data, make it difficult to locate the northern excess in

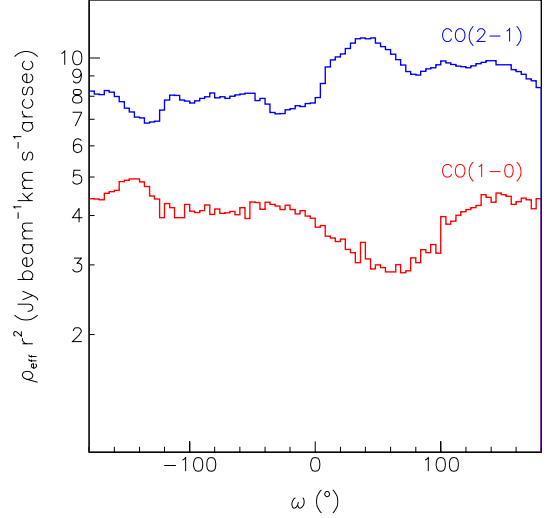


Fig. 10. Distributions of the effective density, multiplied by r^2 , as a function of stellar longitude ω for the annular regions delineated by the rectangles shown in Fig. 8. CO(1–0) data are shown in red, CO(2–1) data in blue.

space precisely. Figure 10 shows the ω distributions of the effective density averaged over the r - α rectangles drawn in Fig. 8 around the maxima of the meridian maps; these distributions do not show an obvious enhancement, the maximum observed in CO(2–1) corresponding in fact to a minimum in CO(1–0). This suggests that the northern excess is distributed over the whole range of stellar longitudes rather than being confined to a particular region in space. This is confirmed by the (y, z) sky maps of the measured fluxes (integrated over Doppler velocity and multiplied by R) that are indicated in Fig. 11 and show an enhancement at radii exceeding $\sim 3''$. This enhancement, which was already noted by Winters et al. (2007) in the case of the narrow velocity component for CO(2–1), is also visible in the broad velocity component. A better space resolution would be necessary to make more quantitative statements concerning this excess, its precise location, morphology, and velocity distribution. The present data allow for a qualitative description, retaining as likely the presence of a northern enhancement at distances from the star exceeding $3''$ and distributed more or less uniformly in stellar longitude.

7. The mean Doppler velocity of the narrow line component

The centroid of the narrow component of the observed spectra moves across the sky map by $\sim \pm 0.5 \text{ km s}^{-1}$ on either side of the average velocity. We measure its mean velocity Δv in each pixel after subtraction of the underlying broad component, interpolated from control regions spanning velocity intervals between 5.4 km s^{-1} and 2.6 km s^{-1} with respect to the average velocity (either blue-shifted or red-shifted). The procedure is illustrated in Fig. 12 for the spectra summed over the $37 \times 37 = 1369$ pixels of the sky map ($9.25'' \times 9.25''$). The resulting Δv distributions, measured in km s^{-1} with respect to the mean velocity measured for the whole maps, are shown in Fig. 13 (left) and their maps are shown in Fig. 14. Both CO(1–0) and CO(2–1) data display very similar features, the narrow component is seen as red-shifted in the north-west direction and blue-shifted in the south-east direction, nearly parallel to the direction of the projected star axis. This suggests that the inclination of the star axis with respect to

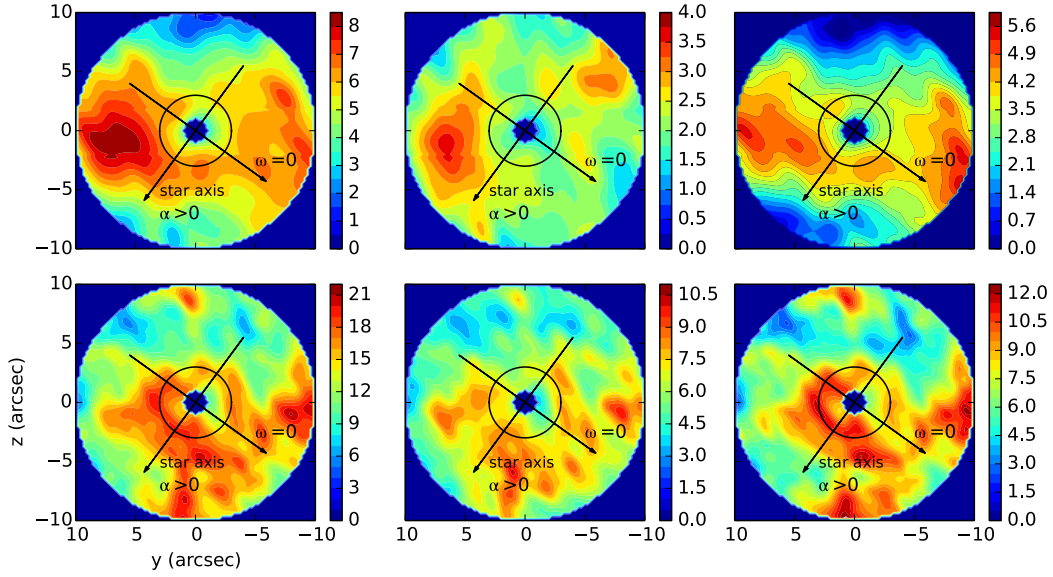


Fig. 11. Sky maps of Rf for CO(1–0) (upper panels) and CO(2–1) (lower panels) observations. Units are $\text{Jy beam}^{-1} \text{ km s}^{-1} \text{ arcsec}$. From left to right: all velocities, $|V_x| < 2 \text{ km s}^{-1}$ and $|V_x| > 2 \text{ km s}^{-1}$. The circles at $R = 3.5''$ correspond to the enhancement seen by Winters et al. (2007) in the narrow velocity component of the CO(2–1) data. The projection of the star axis on the sky plane (making an angle of 13° with the line of sight) and the axis from which the stellar longitude ω is measured (positive clockwise) are shown as black arrows.

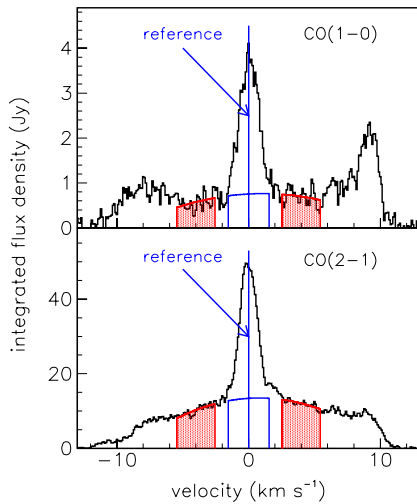


Fig. 12. Illustration of the procedure used to evaluate the mean Doppler velocity Δv of the narrow component. The velocity spectra summed over the 1369 pixels of the map are shown in black for CO(1–0) (upper panel) and CO(2–1) (lower panel). The quadratic fit over the two control regions is shown in red and its interpolation below the narrow component in blue. The vertical blue lines show the mean Doppler velocities of the narrow component from which the interpolated broad component has been subtracted. They are used as reference for separately evaluating Δv in each pixel.

the line of sight, measured by the angle $\theta \sim 13^\circ$, might be the cause of the effect.

To assess the validity of this interpretation quantitatively, we define a band running from south-east to north-west as shown in Fig. 14. Calling ξ the sky coordinate running along the band, we denote in Fig. 13 (right) the dependence of Δv on ξ for pixels contained inside the band. It reveals a complex structure with successive bumps superimposed over a global increase, displaying remarkable similarities between CO(1–0) and CO(2–1), implying that it is likely to be real rather than an artifact of the analysis or instrumental. As a model, we use the best fit

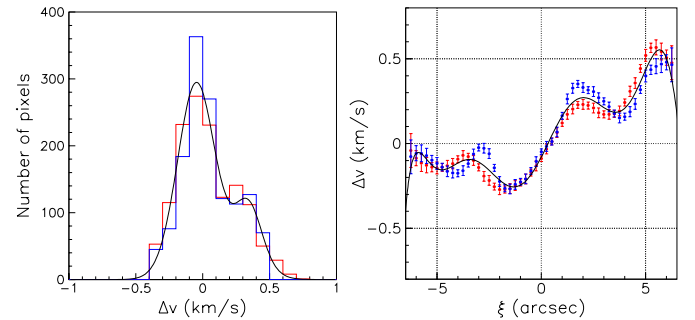


Fig. 13. Left: distributions of the mean Doppler velocity Δv (km s^{-1}) measured with respect to its value averaged over the whole map (shown as “reference” in Fig. 12). The black curve shows a two-Gaussian common fit to the two distributions. Right: dependence of the projection of the mean Doppler velocity Δv (km s^{-1}), averaged over pixels, included in the bands shown in Fig. 14, on coordinate ξ measured from south-east to north-west. The black curve shows a polynomial common fit to the two distributions. In both panels, the CO(1–0) data are shown in red and the CO(2–1) data in blue.

introduced in Sect. 4, however with the temperature distribution and the adjustment of the relative CO(1–0) to CO(2–1) normalization that were introduced in Sect. 5. As illustrated in Figs. 15 and 16, the adopted model correctly reproduces the main features of the observed distributions: the width of the Δv distribution and the amplitude of the Doppler shift when moving from south-east to north-west along the ξ axis. Again, as in the preceding section, observations are well reproduced by the model, not only qualitatively but also quantitatively in their general features. This is only achieved by the hypothesis of a bipolar wind structure and is inconsistent with the assumption of a spherical outflow.

8. Discussion

Applying a bipolar outflow model to analyze the spatially resolved CO(1–0) and CO(2–1) spectra from EP Aqr results in an

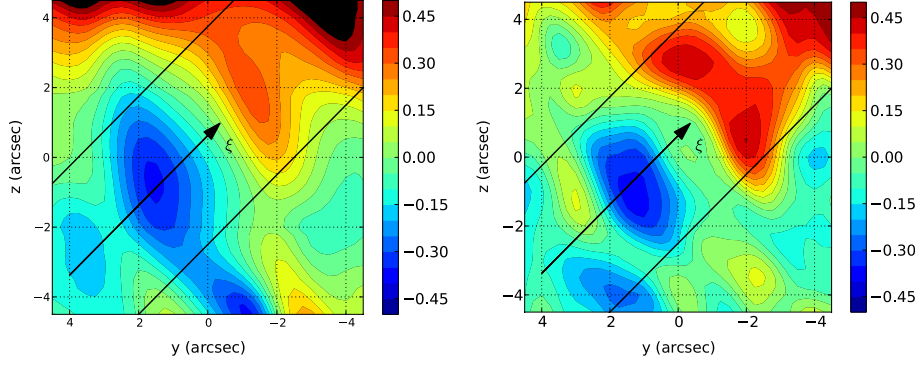


Fig. 14. Sky maps of the mean Doppler velocity Δv (km s^{-1}) measured with respect to its value averaged over the whole map (shown as “reference” in Fig. 12) for CO(1–0) (left) and CO(2–1) (right). The black lines limit the bands in which pixels are retained to evaluate the ξ dependence of Δv (Fig. 13 right).

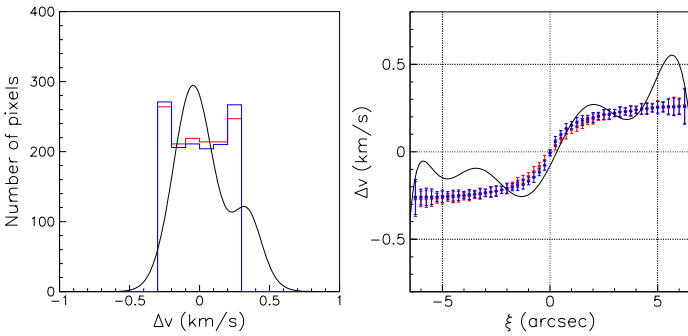


Fig. 15. Results of the model introduced in Sect. 4 for the distributions shown in Fig. 13. The smooth curves are the results of the fits (respectively Gaussian and polynomial) made to the observations in Fig. 13.

excellent agreement of the model results with the observations. The peculiar geometry of the star orientation, with the symmetry axis nearly parallel to the line of sight, implies an approximate circular symmetry when projected on the sky and gives the illusion of a spherically symmetric gas distribution. However, when correlated with the Doppler velocity distributions, it allows for a transparent interpretation in terms of the spatial effective density, and each data-triple is associated with a single point in space once the velocity of the radial wind is known. Under the hypotheses of pure radial expansion and rotation invariance about the star axis, it is possible to reconstruct the space distribution of the effective density. As a first step, we have compared the observations with a simple bipolar outflow model that had been developed earlier to describe another AGB star, RS Cnc. A satisfactory description has been obtained by adjusting the model parameters to best fit the CO(1–0) and CO(2–1) data together. Several parameters defining the morphology and kinematics of the gas volume surrounding EP Aqr have been evaluated this way with good confidence. Among these are the orientation of the star axis, making an angle of $\sim 13^\circ$ with the line of sight and projected on the sky plane at $\sim 144^\circ$ from north towards west. The velocity of the radial wind has been found to increase from $\sim 2 \text{ km s}^{-1}$ at the star equator to $\sim 10 \text{ km s}^{-1}$ at the poles. The flux of matter is also enhanced at the poles, however less than the radial wind, resulting in an effective density slightly enhanced in the equator region. This shows that an axi-symmetry such as that observed in EP Aqr (or RS Cnc; see Fig. 6 in Hoai et al. 2014) is more clearly revealed by velocity-resolved data. For instance, infrared data obtained in the continuum, even at very high spatial resolution, could not reveal this kind of an effect.

This kind of morpho-kinematics could explain that asymmetries in AGB outflows are found preferentially through radio observations obtained at high spectral resolution (e.g. Castro-Carrizo et al. 2010). However, this characteristic of the model is partly arbitrary and its main justification is to provide a good description of the observations. We do not claim that the form adopted in the proposed model is unique; on the contrary, we are confident that other forms could have been chosen with similar success. In particular, the hypothesis of pure radial expansion retained in the model should not be taken as evidence for the absence of rotation of the gas volume about the star axis. Indeed, if it were present, this kind of rotation would be virtually as undetectable as the resulting velocities, as it is nearly perpendicular to the line of sight, and would not produce any significant Doppler shift.

The assumptions made in formulating the model are always approximations, sometimes very crude, of the reality. In particular, evidence has been obtained for significant departures from the symmetry with respect to the star equatorial plane assumed in the model, revealing an excess of emission at northern stellar latitudes over the whole longitudinal range at angular distances from the star exceeding $\sim 3''$. This feature, at least part of it, had already been noted earlier (Winters et al. 2007) and was thought to suggest the existence of successive mass-loss events. In other words, a succession of mass-loss events can be mimicked by a latitudinal variation of the flux of matter.

In general, while the proposed model has been very efficient at describing the main features and general trends of the flux densities, we have also found some significant deviations with respect to the observations. The present data, in particular their spatial resolution, prevent a more detailed statement about the nature of these deviations. An important asset of the model is to illustrate the efficiency of the method used to reconstruct the spatial morphology and kinematics of the gas envelope. Once data of a significantly better resolution are available, e.g. from ALMA, using the same methodology will reveal many of these details with unprecedented reliability and precision.

The availability of measurements of the emission of two different rotation lines of the same gas is extremely precious and has been exploited as much as possible based on the current data. The flux ratio of two lines allows us to evaluate the temperature distribution of the gas in a region where the ratio between the populations and emission probabilities of the two states vary rapidly, which is the case for angular distances from the star probed by the present observations. Most of the details of the model are irrelevant to the value of the flux density

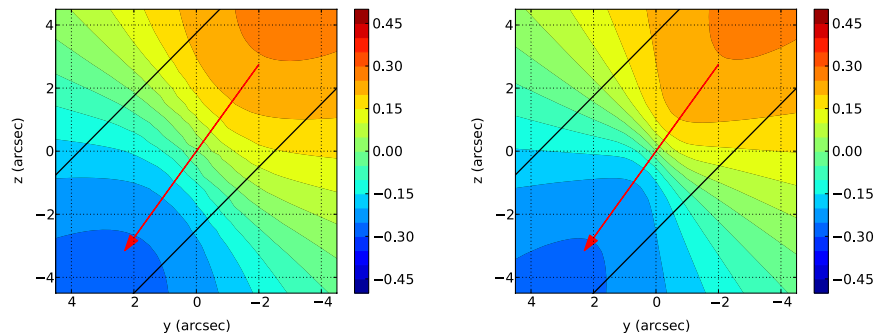


Fig. 16. Results of the model introduced in Sect. 4 for the maps shown in Fig. 14. The red arrows indicate the projection of the star axis on the sky plane.

ratio between the two lines, which depends mostly on temperature under reasonable approximations (local thermal equilibrium, absence of large turbulence, etc.). Through this property, evidence was found for a significant enhancement of temperature at the star equator, therefore, correlated with the orientation of the bipolar flow and at variance with the hypothesis of a pure radial dependence.

We sketched a method in successive steps that allows for iteration of the wind velocity and effective density. When data with significantly improved spatial resolution are available, this will provide a very efficient analysis tool. The peculiar orientation of EP Aqr makes this kind of an analysis much more transparent than in the general case where the star axis is neither parallel nor perpendicular to the sky plane.

Furthermore, the good spectral resolution of the present observations has made it possible to finely analyse the variations of the Doppler velocity of the narrow line component across the sky map, providing a sensitive test of the validity of the bipolar flow hypothesis and a quantitative check of the inclination of the star axis with respect to the line of sight.

The present work leads us to prefer a bipolar, stationary, wind model over the spherical, variable scenario that was proposed earlier. AGB stars have traditionally been assumed to be surrounded by nearly spherical circumstellar shells. Deviations, sometimes spectacular, from spherical symmetry are observed in planetary nebulae (PNs). These deviations are also observed in post-AGB sources and it is generally considered that they arise during the phase of intense mass loss after the central stars have evolved away from the AGB. However, it has also been recognized that the geometry of circumstellar shells around AGB stars may sometimes show an axi-symmetry (e.g. X Her, Kahane & Jura 1996; RS Cnc, Hoai et al. 2014). The origin of this axi-symmetry has not been clearly identified: the magnetic field, stellar rotation, or presence of a close binary companion may play a role. Recently, Kervella et al. (2015) reported the detection of a companion to L2 Pup, another M-type AGB star, with a disk seen almost edge-on. The case of EP Aqr is particularly interesting because, with no detected Tc and a $^{12}\text{C}/^{13}\text{C}$ ratio ~ 10 , it seems to be in a very early stage on the AGB. All these cases raise the interesting possibility that the deviations from sphericity observed in PNs and in post-AGB stars are rooted in their previous evolution on the AGB.

9. Conclusion

We have revisited the EP Aqr data obtained by Winters et al. (2007). We now interpret them in terms of an axi-symmetrical

model similar to that developed for RS Cnc by Hoai et al. (2014). The expansion velocity varies smoothly with latitude, from $\sim 2 \text{ km s}^{-1}$ in the equatorial plane to $\sim 10 \text{ km s}^{-1}$ along the polar axis, which for EP Aqr is almost parallel to the line of sight. The mass-loss rate is estimated at $\sim 1.2 \times 10^{-7} M_{\odot} \text{ yr}^{-1}$. The two stars look very similar, as the differences in the observations are only an effect of the orientations of their polar axis with respect to the line of sight. There is evidence for a temperature enhancement near the star equator and a faster decrease along the polar axis than in the equatorial plane.

Both RS Cnc and EP Aqr show peculiar CO line emission whose profiles consist of two components (Knapp et al. 1998; Winters et al. 2003). This may suggest that the other sources with these kinds of composite CO line profiles (e.g. X Her, SV Psc, etc.) might also be interpreted with a similar model, rather than with successive winds of different characteristics as has been proposed earlier.

Acknowledgements. This work was done in the wake of an earlier study, the results of which have been published (Winters et al. 2007). We thank those who contributed to it initially, in the phases of design, observations, and data reduction for having encouraged us to revisit the original analysis in new terms. Financial support from the World Laboratory, from the French CNRS in the form of the Vietnam/IN2P3 LIA and the ASA projects, from FVPPL, from PCMI, from the Viet Nam National Satellite Centre, from the Vietnam National Foundation for Science and Technology Development (NAFOSTED) under grant number 103.08-2012.34 and from the Rencontres du Vietnam is gratefully acknowledged. One of us (DTH) acknowledges support from the French Embassy in Ha Noi. This research has made use of the SIMBAD and ADS databases.

References

- Cami, J., Yamamura, I., de Jong, T., et al. 2000, *A&A*, **360**, 562
- Castro-Carrizo, A., Quintana-Lacaci, G., Neri, R., et al. 2010, *A&A*, **523**, A59
- Cox, N. L. J., Kerschbaum, F., van Marle, A.-J., et al. 2012, *A&A*, **537**, A35
- Hoai, D. T., Matthews, L. D., Winters, J. M., et al. 2014, *A&A*, **565**, A54
- Kahane, C., & Jura, M. 1996, *A&A*, **310**, 952
- Kervella, P., Montargès, M., Lagarde, E., et al. 2015, *A&A*, **578**, A77
- Knapp, G. R., Young, K., Lee, E., & Jorissen, A. 1998, *ApJS*, **117**, 209
- Le Bertre, T., & Gérard, E. 2004, *A&A*, **419**, 549
- Lebzelter, T., & Hron, J. 1999, *A&A*, **351**, 533
- Mamon, G. A., Glassgold, A. E., & Huggins, P. J. 1988, *ApJ*, **328**, 797
- Nakashima, J. 2006, *ApJ*, **638**, 1041
- Nhung, P. T., Hoai, D. T., Winters, J. M., et al. 2015, *RA&A*, **15**, 713
- Tuan Anh, P., Diep, P. N., Hoai, D. T., et al. 2015, *RA&A*, in press [[arXiv:1503.00858](https://arxiv.org/abs/1503.00858)]
- van Leeuwen, F. 2007, HIPPARCOS, the New Reduction of the Raw Data (Springer), *Astrophys. Space Sci. Lib.*, **350**
- Winters, J. M., Le Bertre, T., Jeong, K. S., Nyman, L.-Å., & Epchtein, N. 2003, *A&A*, **409**, 715
- Winters, J. M., Le Bertre, T., Pety, J., & Neri, R. 2007, *A&A*, **475**, 559